Selective laser melting of Fe-Al alloys with simultaneous gradients in composition and microstructure

Siyuan Wei [a], Kwang Boon Lau [b], Jing Jun Lee [b], Fengxia Wei [b], Wei Hock Teh [b], Baicheng Zhang [c], Cheng Cheh Tan [b], Pei Wang [b,*], Upadrasta Ramamurty [a,b]

[a] *School of Mechanical and Aerospace Engineering, Nanyang Technological University, Singapore 639798, Republic of Singapore*
[b] *Institute of Materials Research and Engineering, Agency for Science, Technology and Research, 2 Fusionopolis Way, Singapore 138634, Republic of Singapore*
[c] *Advanced Material & Technology Institute, University of Science and Technology Beijing, Beijing, 100083, P.R. China*

*Corresponding author: wangp@imre.a-star.edu.sg

Abstract: Selective laser melting technique was employed to fabricate a step-wise compositionally graded Fe-Al alloy coupon using the in-situ alloying of blended powders. Microstructural characterization of the fabricated coupons shows a columnar to equiaxed grain structure transition with increasing Al content along the building direction, along which the laser scan speed is increased. In the low Al content regions, the absence of constitutional undercooling (CUC) allows columnar grain growth against the macroscopic thermal gradients, whereas dominance of CUC in high Al regions leads to fully equiaxed and refined microstructures. Nanoindentation studies show a linear increase in hardness and reduction in elastic modulus for Al content up to ~20 at.%; no significant anisotropy in these properties could be seen.

Keywords: Selective laser melting; Iron alloy; Solidification microstructure; Undercooling; Columnar to equiaxed transition; Nanoindentation.

----

1. Introduction

Among the many advantages offered by metallic component additive manufacturing (AM), by using methods such as selective laser melting (SLM) of powder beds, *in-situ* alloying and compositional gradation are considered to have significant potential[1]. However, their ability to identify new alloys with chemistries that were not examined hitherto or generate components with unique functional and/or mechanical property gradations remains relatively unexplored. While compositionally graded materials are recently fabricated by combining two different well-established engineering alloys, *e.g.*, stainless steel 304L/Inconel 625 [2], Co29Cr6Mo/Inconel 718 [3], and TiC/Ti [4], metal component AM wherein both *in-situ* alloying with graded composition were simultaneously exploited, was not examined. Keeping this in view, SLM of step-wise graded binary Fe-Al alloy coupon fabrication was investigated in this work.

The Fe-Al alloy system is a widely explored one[5, 6], especially due to the possibility it offers in terms of enhancing the specific properties of steels [7-9]. Conventional manufacturing of Fe-Al alloy components is, however, challenging since these alloys are not as easily amenable to thermomechanical processing as 'regular' steels[10]. While processing steps such as forging and rolling are completely circumvented during AM, SLM of alloys with high Al content is difficult due to cracking, particularly when elemental Fe and Al powders are used as feedstock [9, 11, 12]. Therefore, recent studies have focused on the fabrication of pre-alloyed Fe-Al alloys [9, 13]. Thus, another objective of this work is to ascertain the maximum Al content that would enable crack-free coupon fabrication using SLM. A final objective is to examine the gradation in the microstructures with the Al content, to gain insights into the grain structure formation during AM. While gradients in both prior β grain width and β phase interspacing in Ti-6Al-4V alloy [14], and grain size with composition in Fe-FeAl alloys [15] were reported, mechanistic origins for such were yet to be ascertained.

2. Material and methods

Commercially available Fe (average diameter 22.8 ± 2.5 μm) and Al (average diameter 26.9 ± 12.7 μm) powders are used to fabricate step-wise graded Fe-Al coupons on SS316L substrate. Powder mixtures corresponding to six different compositions (Table 1) are blended using a customized mill that rotated at a rate of 150 rpm for 23 h and air-dried before being utilized for fabricating the graded coupons in a Trumpf Truprint 1000 SLM machine. The 3 (width), 5 (thickness), and 30 mm (height) sized specimens were fabricated by first printing a 5 mm high alloy with the first composition, then another 5 mm on top with the next composition, and so on. While the laser power (w = 175 W), hatch distance (l = 100 μm), layer thickness (t = 30 μm), and scan rotation between the successive layers (ϕ = 67°) remained unaltered for all the six compositions, the scan speed (v) was varied from 300 to 800 mm/s, to obtain dense samples with minimum porosity. (The optimum v for each composition were arrived at after several trials on single composition builds.) The energy density, $J = w/lvt$, for each composition along with *v* are listed in Table 1. After the fabrication, the coupons were sectioned parallel to the build direction and were mechanically mirror polished for microstructural and mechanical property characterization.

Table 1. Compositions of the alloy and microstructural phase expected (from the phase diagram on the basis of the composition) to be present at different regions of the graded Fe-Al alloy coupon fabricated using selective laser melting. The scan speed (and the corresponding energy density) used for the fabrication of different regions are listed. Rest of the process parameters were unchanged across the entire coupon.

Region	**Nominal Al content (at.%)**	**Measured Al content (at.%)**	**Expected microstructural phase**	**Scan speed, *v* (mm/s)**	**Energy density, *J* (J/mm^3)**
1	9.8	6.2 ± 0.5	A2 (Fe-Al solid solution)	300	194.4
2	18.7	15.1 ± 0.6	ibid	400	145.8
3	26.8	23.9 ± 0.7	$D0_3$ (Ordered intermetallic phase: Fe_3Al)	500	116.7
4	34.1	32.1 ± 0.8	B2 (Ordered intermetallic phase: FeAl)	600	97.2
5	37.5	35.4 ± 1.9	ibid	700	83.3
6	40.8	39.1 ± 2.1	ibid	800	72.9

X-Ray diffraction (XRD, Bruker D8 Discover) using a Cu source, energy-dispersive X-Ray spectroscopy (EDS), backscattered electron (BSE) imaging and electron backscatter diffraction (EBSD) with inverse pole figure (IPF) mapping using a scanning electron microscope (SEM, JEOL 7600F) were utilized to study the chemical, phase, and microstructure variations in the fabricated specimens. Mechanical characterization was performed using a nanoindenter (Bruker TI 980) and a Vickers microhardness tester (FM-300e). 20 nanoindentations with a Berkovich tip were conducted for each composition, with a peak load of 10 mN, loading and unloading rates of 1 mN/s, and a hold time of 2 s at the peak load.

3. Results

3.1. Microstructures

The compositional variation across the fabricated coupons, evaluated using EDS mapping, is displayed in Fig. 1. Within each of the six regions, the Al content is comparatively uniform, confirming good blending of the Fe and Al powders and no macroscopic segregation during printing. However, the realized Al content in the printed samples is lower (by 2 to 3.6 at.%) than those of the blends (Table 1); in terms of the relative amount of Al loss during SLM, regions 1 to 3 appear to be particularly affected. This lost can be ascribed to the vaporization of Al (similar phenomenon was reported by Kang et al. [16]), which decreases with increasing v and J. Microscopic examination of the builds showed they are crack-free (except for the last region of 6), which indicates that it might be possible to incorporate up to 35 at.% Al in Fe using the SLM strategy. Relative densities of the six regions, estimated using the optical micrographs, are: 99.2 ± 0.3%, 99.2 ± 0.4%, 98.9 ± 0.6%, 98.5 ± 0.5%, 98.1 ± 0.7% and 97.4 ± 0.7%, respectively.

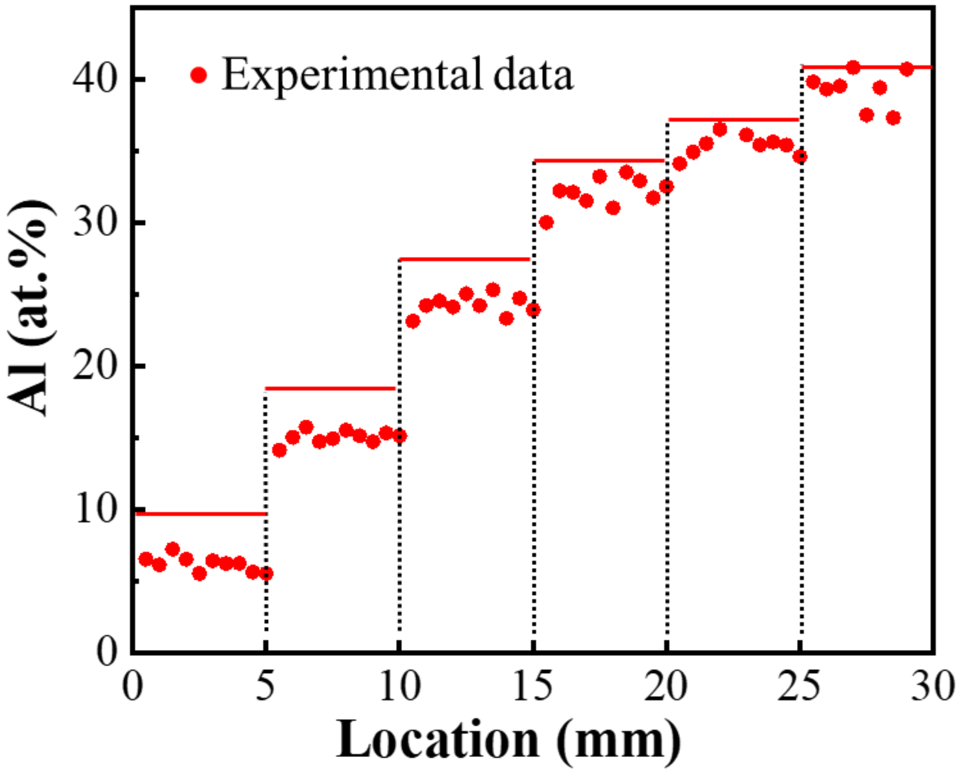

Figure 1. Al content against locations of graded sample, based on EDS. Red dots indicate measured Al contents at the corresponding locations. Black dashed lines and red bars indicate the region interfaces and expected Al contents, respectively.

The variation of microstructure and texture across a fabricated graded Fe-Al alloy coupon are displayed in Figs. 2a-b. In both regions 1 and 2, <001> oriented columnar grains can be seen. This is not surprising given that <001> is the easy growth direction for alloys with the body centered cubic (BCC) structure. When the Al content is increased in region 3, an abrupt columnar to equiaxed transition is seen. Further increases in the Al content leads to progressive refinement of the grains and randomization of their orientations. The texture evolution in the fabricated coupon with the Al content is illustrated in Fig. 3 through IPFs obtained at each of the locations and obtained on cross-sections normal to the build, transverse, and normal directions (BD, TD, and ND respectively). In all the three orientations, the texture intensity drops as the Al content increases; a sharp reduction the maximum intensity between region 2 and 3 in the BD orientation is seen whereas the reduction is more gradual in the other two orientations. The texture strengths between TD and ND in all the six regions are similar, but are much smaller than those seen along BD. If the ratio of the maximum intensities is considered as an indicator of the microstructural anisotropy, then alloy in regions 1-2 is highly anisotropic. Progressive reduction in the anisotropy with the Al content can be seen, culminating in a near-isotropic material in region 6.

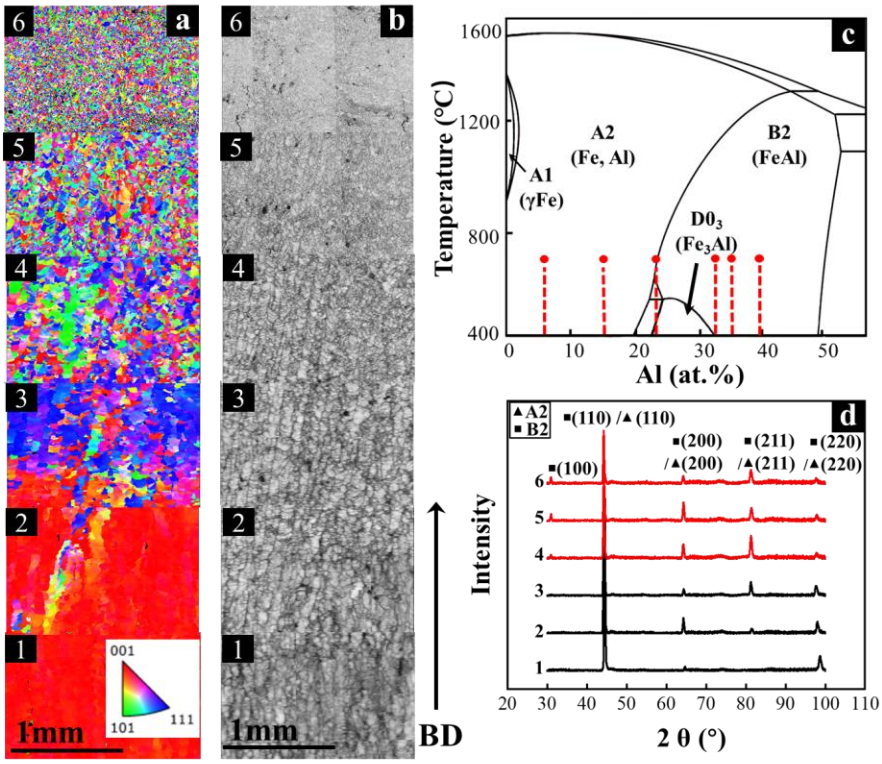

Figure 2. (a) Electron backscatter diffraction (EBSD) and (b) backscattered electron (BSE) images showing the microstructural variation across the entire graded coupon along the build direction (BD). (c) The Fe-rich side of the Fe-Al phase diagram (adapted from [17]). The Al contents of the six regions are marked on it with red dashed lines. (d) XRD scans obtained from the six regions.

The binary Fe-Al phase diagram is displayed in Fig. 2c with the measured compositions of the six regions marked on it. As seen from it, the following three equilibrium phases are possible at room temperature within the composition range examined in this work: (i) disordered Fe and Al solid solution with BCC crystal structure, referred to as A2, (ii) ordered B2 FeAl intermetallic phase, and (iii) ordered intermetallic phases with Fe_3Al stoichiometry and referred to as $D0_3$. For each of the six compositions used, the expected phase(s) in the microstructure within the corresponding region, is (are) listed in Table 1. The XRD patterns obtained from each of the six regions are displayed in Fig. 2d. Analysis of these patterns shows that while the expected phases (A2 and B2) are present in regions 1-3 and 4-6, respectively, no signature of the $D0_3$ phase, which is expected in location 3 could be seen. It is also worth noting that the diffraction peak corresponding to the {211} planes in location 1 is missing, which is possibly due to the strong texture in that region.

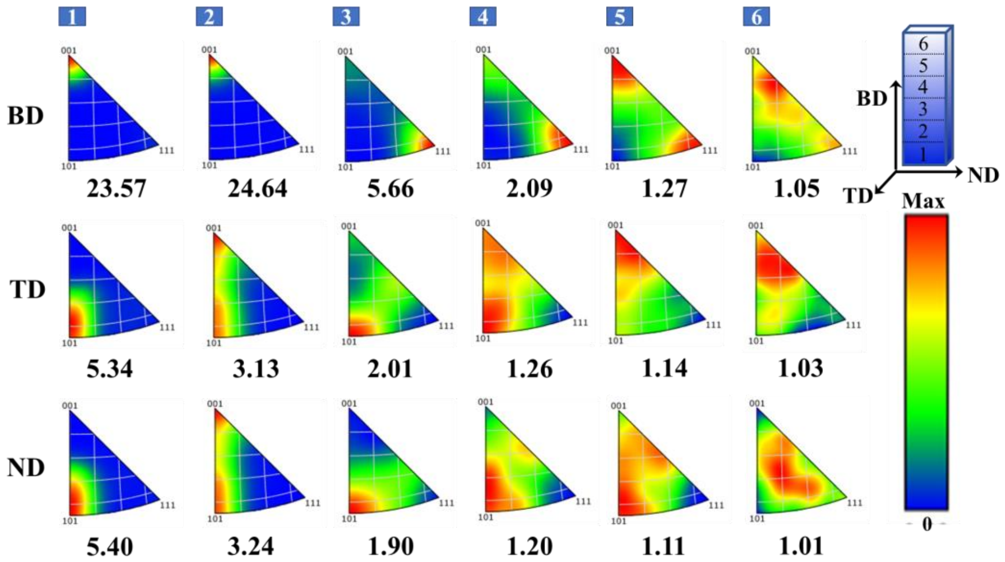

Figure 3. IPF images in six locations along build, transverse and normal directions (BD, TD and ND respectively). Numbers show the maximum intensity of each IPF figure.

Higher magnification BSE micrographs obtained from the six regions are displayed in Fig. 4. Figs. 4a-b, obtained from regions 1 and 2 respectively, show that the columnar grains grow along BD and across the melt pools, with a marginal grain refinement in region 2. The coarse columnar grains are broken into smaller ones upon entering region 3 (Fig. 4c), with the direction of the grain shifting towards the center of the melt pool. The ratio of non-columnar grains increases continuously in regions 4 to 6, and progressive columnar-to-equiaxed transition (CET) occurs. Several intergranular cracks are observed in region 6 (Fig. 5).

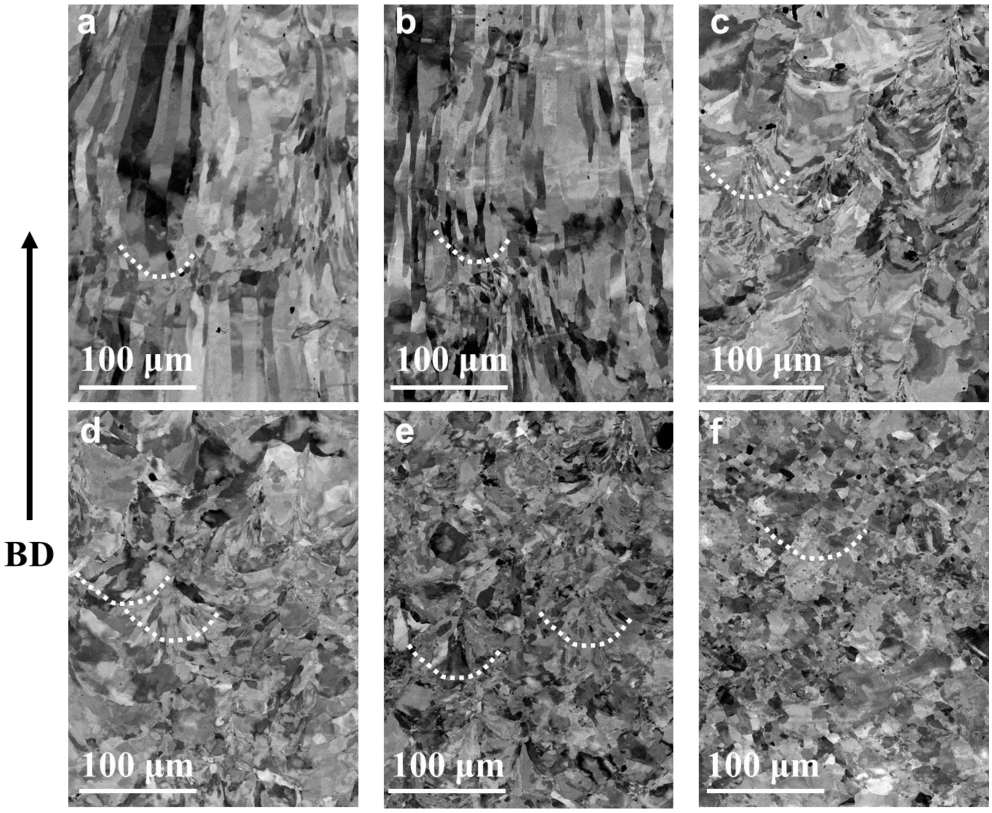

Figure 4. Representative BSE micrographs obtained from the six different locations showing the microstructural features along the build direction (BD, which is indicated with the arrow). White dashed lines highlight representative melt pool boundaries.

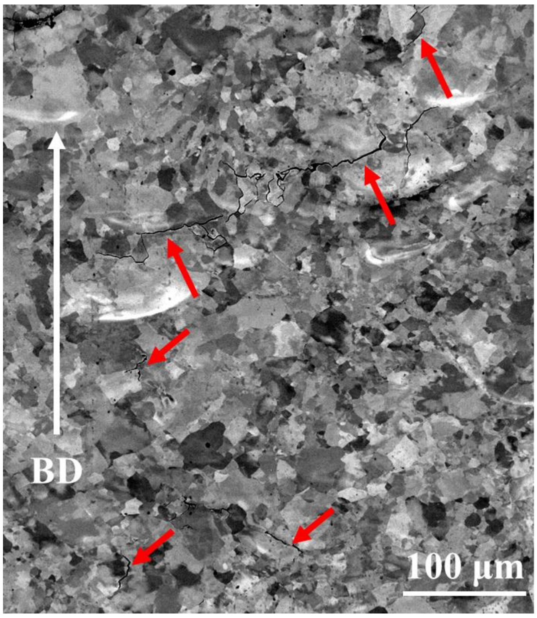

Figure 5. Representative BSE micrographs obtained from region 6. Red arrows highlight cracks formed during the fabrication.

Higher magnification IPF micrographs are further used to study the microstructure and grain size variations, as demonstrated in Figs. 6a-f. In regions 1-2, epitaxial growth along <001> direction predominates, which, in turn, suppresses the nucleation and growth of grains that are randomly orientated, resulting in the uniformly aligned columnar grains in Figs. 6a-b. Combining IPF and BSE results in region 3 (Fig. 4c and 6c), it is surmised that instead of columnar grains that grow across melt pools, confined grain growth that is still aligned occurs, resulting in the change of overall orientation. When the content of Al further increases from regions 4 to 6, randomization of the grain orientation occurs; it appears that grains with random orientations nucleate along the melt pool boundaries and grow with progressive refinement of the grain structures with an increasing Al content.

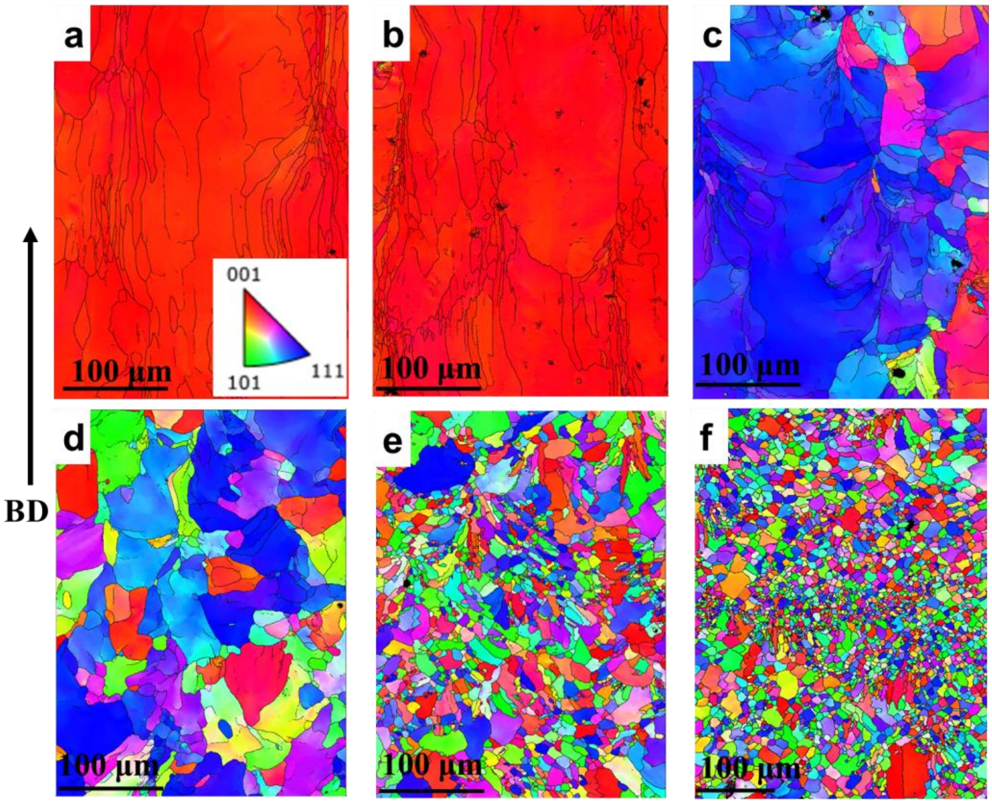

Figure 6. Representative EBSD IPF images from the six locations showing the grain morphology and texture.

3.2. Mechanical properties

The variations of Young's modulus, *E*, and hardness, *NH* (nanoindentation hardness), measured using nanoindentation on cross-sectional planes, whose normal directions coincide with either BD or TD, of the six regions are plotted in Fig. 7, as a function of the Al content. Measured variations of the Vickers hardness (VH) are also plotted. For comparison purposes, respective properties measured on an unalloyed Fe block (printed with the same process parameter combinations) are also plotted. The following are some observations. (a) While NH is much higher than VH, which is commonly observed, the trends in both are similar. (b) Both NH and VH increase, relatively steeply for up to 20 at.% Al and then more gradually, with the Al content in the alloy. (c) For pure Fe and regions 1-2, a linear reduction in E is noted. Persistent—but not significant (< 3%)—anisotropy with E in TD being always higher, was noted. A marked reduction of E in TD and significant anisotropy are noted in region 3; these are possibly due to partial formation of $D0_3$ phase [18]. E increases again in regions 4-5. (d) Both E and hardness in region 6 are lower than the respective values in 5, presumably due to the cracking. Overall, the anisotropy in mechanical properties is insignificant.

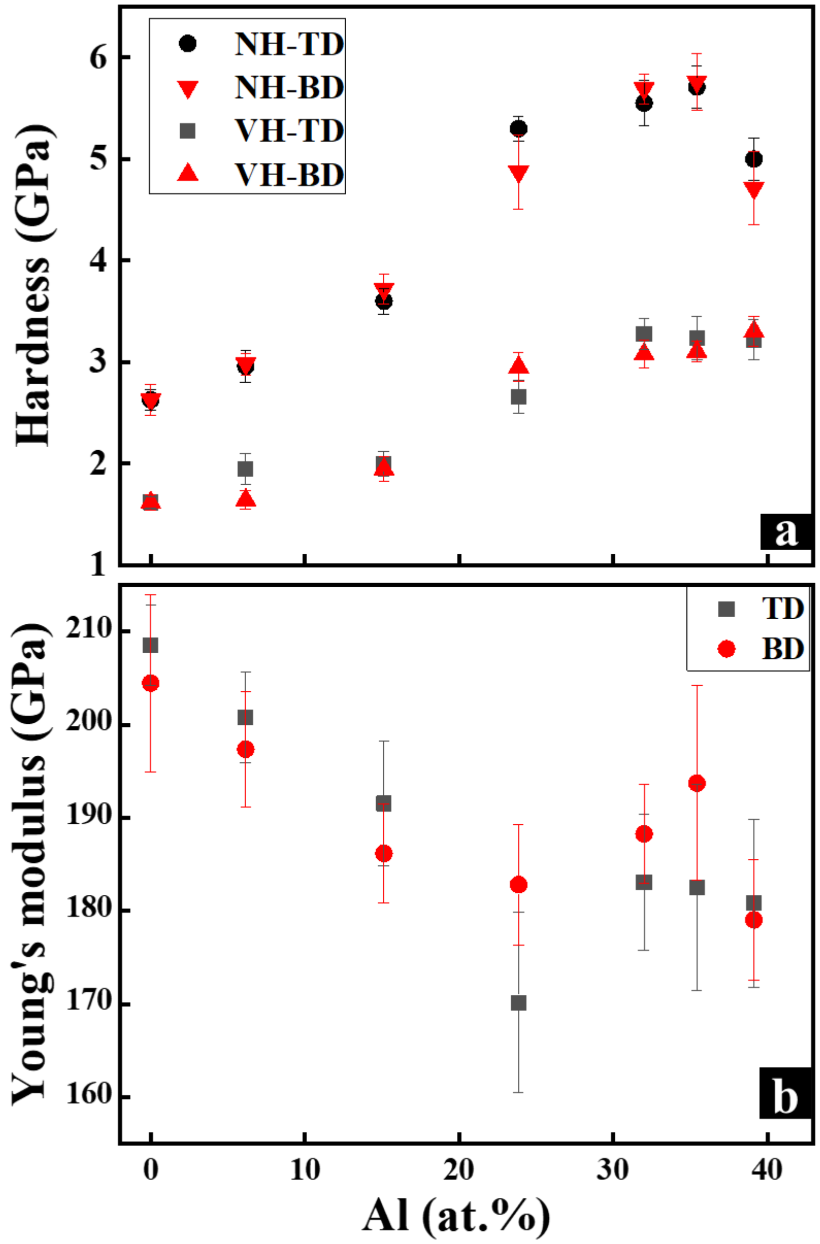

Figure 7. Variations of (a) hardness values measured with nanoindentation (NH) and micro-indentation (VH) and (b) Young's modulus, *E* (measured with nanoindentation) with the Al content in the alloy. These mechanical properties were measured on the planes with the plane-normal oriented along the build direction (BD) or transverse to the build direction (TD).

4. Discussion

4.1. Compositional dependence of the microstructure

During the layer-by-layer deposition that is common in most AM processes, columnar grains are typically favored due to the small energy barrier of epitaxial growth [19, 20].

Moreover, grains, whose growth direction is parallel to the thermal gradient direction, can overgrow their misaligned counterparts [21]. Since the thermal gradient direction is typically aligned with BD, columnar grains along BD are prevalent in AM fabricated metals and alloys with uniform chemical composition. However, when dissimilar metals are used, for example in laser surface cladding or for the fabrication of compositionally graded materials, local dynamics of solidification and grain nucleation will be disparate. The underlying mechanisms for both CET and grain refinement in the graded Fe-Al alloy observed in the present study could be due to constitutional undercooling (CUC) that is intrinsic to the alloy system, as following.

The critical condition that needs to be satisfied for CUC, which is the driving force for dendrite growth, can be expressed as [22],

$$\frac{G}{R} \leq m\frac{c_0}{D}\left(\frac{K_0 - 1}{K_0}\right) \tag{1}$$

where G is the thermal gradient, R is the solidification velocity, m is the slope of the liquidus in the phase diagram, c_0 is the solute content in the alloy, and D and K_0 are diffusion and partition coefficients, respectively. As seen from it, the G/R is the predominant factor that determines the solidification mode in both conventional and AM processes [23-25]. In the former, with decreasing G/R, the solidified microstructure transitions from planar to cellular dendritic and then to equiaxed dendritic [21]. In SLM, CET is also found to be related to low G/R, induced by higher v [26], and is ascribed to an increase in CUC [21]. As mentioned already, v was varied for each of the six compositions while fabricating the graded coupon in the present study. With an increase in the Al content, v was increased (Table 1). Hence, it is reasonable to assume that G/R in the graded Fe-Al alloy coupon decreases progressively along BD.

Since G/R values are not available, utilizing Eq. 1 for a quantitative evaluation of CUC is not possible. It has been suggested recently that the growth restriction factor (Q) can be used for estimating CUC in metallic components fabricated by AM process [27]. In the theory of solidification, it is suggested that the segregation of solutes exerts a significant effect on the grain morphology and size. The concept of Q is developed to evaluate the degree of segregation, which indicates the restricting effect of solute on the growth of solid-liquid interface of the new grains [28]. This approach was validated on several different Ti-based alloys, *e.g.*, Ti-Cu [27], Ti-W [29] and Ti-Al-V-Fe [30], in which high values of Q are found to induce formation of fine equiaxed grains. It is argued in these studies that high Q value provides sufficient CUC, which can suppress the tendency of epitaxial growth induced by high thermal gradient; in such case, complete CET can be triggered [27]. The value of Q can be estimated using the following equation:

$$Q = mc_0(K_0 - 1) \quad , \tag{2}$$

where m, c_0, and K_0 are the slope of the liquidus in the phase diagram, the solute content in the alloy, and the partition coefficient, respectively. The parameters on the right-hand side of the above equation are inherent to each of the alloy and are sensitive to composition, which can be calculated based on Fe-Al binary phase diagram (Fig. 2c). Hence, the effect of Al content on CUC is quantitatively discussed here, on the basis of the calculated Q and average grain size d (Fig. 8). As seen from Fig. 8a, d remains similar in regions 1-2 and then decreases progressively with the increasing Al content in regions 3-6. As for Q, in region 1 of the graded SLM coupon, m is close to 0, therefore, Q is ~ 0 °C; then, with increasing Al content, Q keeps growing to a maximum value of ~28.7 °C in region 6. It is also worth noting that the incremental rate is insignificant in regions 1-2 and then becomes more drastic in regions 3-6.

As reported in recent studies, the level of CUC (ΔT_{CUC}) is proportional to Q through the dimensionless super-saturation parameter (Ω) [27, 31]:

$$\Delta T_{CUC} = Q\Omega. \tag{3}$$

The above equation indicates that ΔT_{CUC} increases more than 30 times as the Al content increases from region 2 to 6. This significant increase of ΔT_{CUC} markedly contributes to the CET and refinement of grain size. From the observation of grain morphology in Figs. 4-6, an approximate estimate of the Al content, which can induce initiation and completion of CET in Fe-Al alloys fabricated by AM process, is marked out by blue dashed lines in Fig. 8a. Moreover, critical Q which allows for CET to be completed can be estimated to be ~28 °C. To further study the effect of CUC on the grain size, 1/d is plotted against Q in Fig. 8b. As seen from it, 1/d increase exponentially with Q, which means certain amount of Q is needed to substantially refine the grain size.

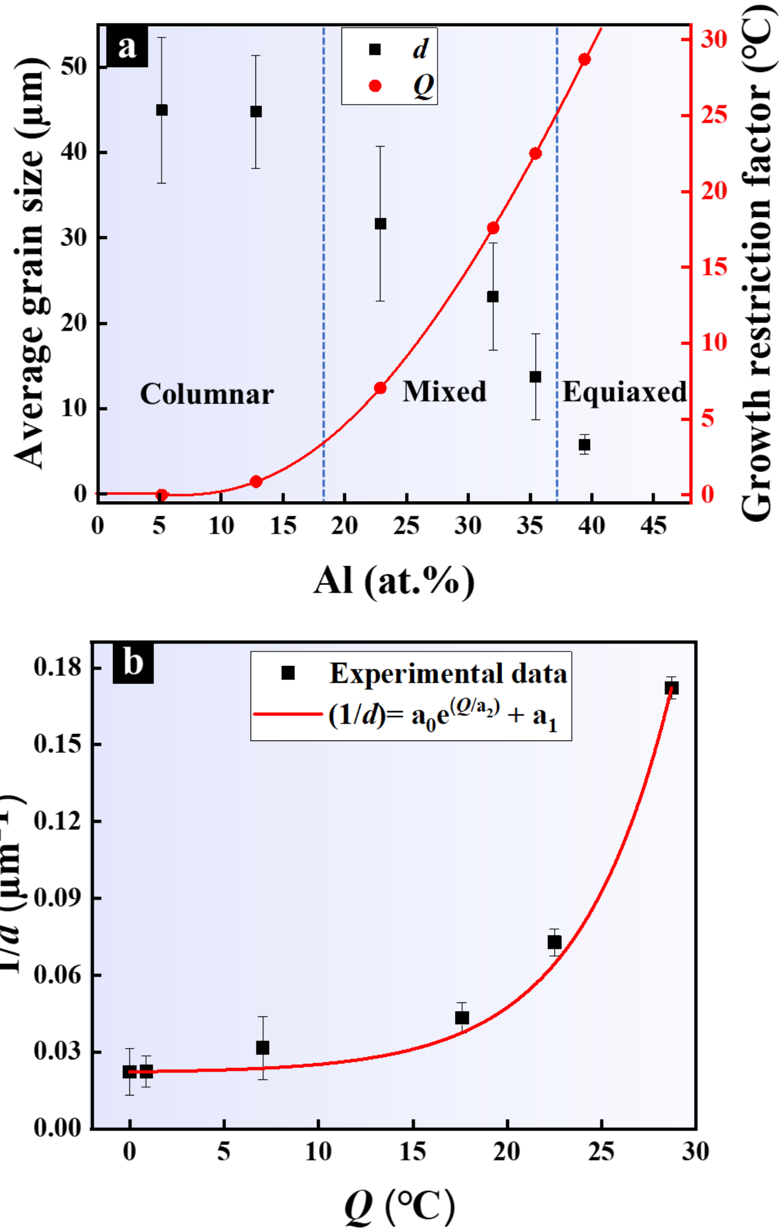

Figure 8. (a) Variations of average grain size d (equivalent circular diameter, obtained from EBSD) and growth restriction factor Q with the Al content in the alloy. (b) Plot of $1/d$ against Q. Constants a_0, a_1 and a_2 equal to 4.38×10^{-4} μm^{-1}, 0.02 μm^{-1} and 4.91 °C, respectively.

4.2. Model for the grain morphology evolution

As CUC does not occur in regions 1-2, nucleation of equiaxed grains ahead of the solidification front is suppressed. Since the substrate serves as the main heat sink, the thermal gradient is aligned along BD, growth of coarse <001>-oriented columnar grains along BD is favored, as schematically illustrated in Fig. 9a. As the Al content is increased, Q and ΔT_{CUC} increase. This, in addition to a reduction in G/R (due to increased v), leads to an enhanced CUC with increasing Al content, which, in turn, provides the necessary driving force for grain nucleation with increasing rate. Hence, progressive grain refinement with the Al content in regions 3 onwards is seen. Thus, instead of epitaxial growth, small columnar grains, which nucleate at the melt pool boundaries, grow first against the local dominating thermal gradient: towards the center of the melt pool (Fig. 9b). Upon a further increase in the Al content in regions 5-6, a further transition into an ideal morphology of fully equiaxed grains within each melt pool, where new grains nucleate at the boundaries of the solidified ones occurs (Fig. 9c). In this context, it is interesting to note that such mode of solidification is rather rare in components fabricated by SLM, which requires specific technique to minimize the energy barrier for nucleation. For example, nanoparticles and intragranular nanoprecipitation were introduced in SLM to serve as heterogeneous nucleation sites to fabricate significantly refined microstructures [12, 32].

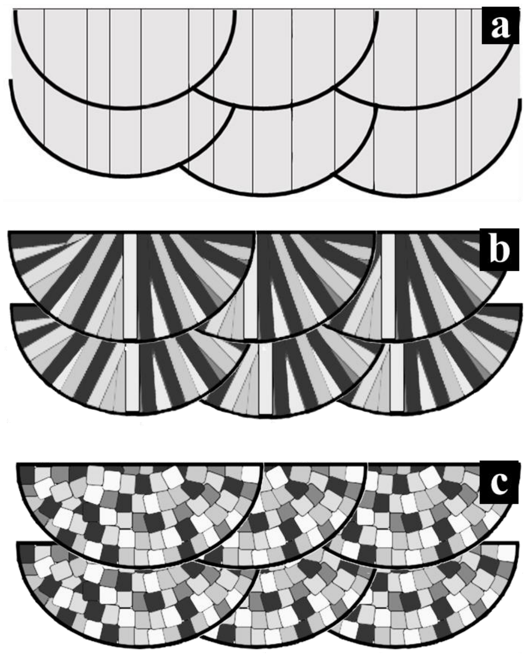

Figure 9. Schematic illustrations of the grain morphology evolution within each melt pool and across several melt pools during selective laser melting with (a) negligible constitutional undercooling (CUC) leading to highly textured, columnar grain growth across the melt pools and in the direction opposite to that of the macroscopic thermal gradient, (b) growth of grains, which nucleated a the melt pool boundaries, towards the center of the melt pools due to some CUC, and (c) fully-equiaxed microstructure due to the dominance of CUC.

Among Fe-rich Fe-Al alloys/intermetallics, the lowest *E* is typically observed when the $D0_3$ phase forms and increases steadily with the formation of B2 phase [33], presumably due to the replacement of Fe-Fe bonds by Fe-Al bonds, lattice ordering, and magnetic effects. Keeping this in mind, both XRD (Fig. 1d) and the mechanical property measurements (Fig. 7) suggest the complete formation of B2 in regions 4-6, and $D0_3$ partially in region 3. These phase transformations occurred in regions where progressive CET occurs; in this context, it is interesting to note that researchers in a recent study speculated causal relationship between them [15]. Since solidification occurs prior to phase transformation and the difference in the lattice parameters of A2 and B2 phases is negligible (~ 0.29%), phase transformation should not have significant influence on the morphology of solidified grains. Also, given $D0_3$ phase is only partially transformed in region 3, its effect on the CET should be minimum. Detailed tensile and fracture property characterization of the different SLM Fe-Al alloy coupons, to especially ascertain their brittleness as a function of the Al content, is currently underway.

5. Summary

Compositionally graded Fe-Al alloy coupons were fabricated using the SLM technique, to explore the maximum Al content that can be accommodated in Fe without cracking. Microstructural characterization shows that, with an increasing Al content and scan speed along BD, a transition from columnar to equiaxed microstructure, which was followed by progressive grain refinement, occurs. These transitions are ascribed to the constitutional undercooling, which provides the necessary driving force for the growth of dendrites and affects the morphology and size of the solidification microstructures. Here, *Q* is found to be applicable to evaluate the CUC in Fe-Al alloys, which is sensitive to Al content. It is approximately estimated here that the Al content where CET initiates is ~18 at.%. Further quantitative study shows that refinement of *d* is closely associated with *Q*, where *1/d* increases exponentially with it. The critical *Q* value, which allows for complete CET is found to be ~28 °C. Mechanical property evaluation performed via the nanoindentation technique across the graded coupon shows a gradual reduction in the elastic modulus and a linear increase in hardness for up to ~23 at.% Al. In spite of a significant anisotropy in texture, mechanical anisotropy was found to be minimal. The combination of microstructural and mechanical property studies indicates that an Al content that ranges between ~18 and 23 at.% would be suitable for additive manufacturing of Fe-Al alloys using selective laser melting.

CRediT authorship contribution statement

Siyuan Wei: Investigation, Writing - Original Draft, Writing - Review & Editing. **Kwang Boon Lau:** Investigation. **Jing Jun Lee:** Investigation. **Fengxia Wei:** Investigation. **Wei Hock Teh:** Investigation. **Baicheng Zhang:** Conceptualization. **Cheng Cheh Tan:** Conceptualization. **Pei Wang:** Conceptualization, Methodology, Funding acquisition, Supervision, **Upadrasta. Ramamurty:** Conceptualization, Funding acquisition, Supervision, Writing - Review & Editing.

Acknowledgements

This work was funded through the Structural Metal Alloys Program (Grant reference No.: A18b1B0061) of the Agency for Science, Technology and Research of Singapore**.** The authors gratefully thank the technical support on EBSD analysis from Dr Hwee Leng Seng and nano-indentation analysis from Mr. Tzee Luai Meng of IMRE.

Data Availability

The data that support the findings of this study are available from the corresponding author on reasonable request.

References

[1] S. Huang, R.L. Narayan, J.H.K. Tan, S.L. Sing, W.Y. Yeong, Resolving the porosity-unmelted inclusion dilemma during in-situ alloying of Ti34Nb via laser powder bed fusion, Acta Mater. 204 (2021), https://doi.org/10.1016/j.actamat.2020.116522.
[2] B.E. Carroll, R.A. Otis, J.P. Borgonia, J.-o. Suh, R.P. Dillon, A.A. Shapiro, D.C. Hofmann, Z.-K. Liu, A.M. Beese, Functionally graded material of 304L stainless steel and inconel 625 fabricated by directed energy deposition: Characterization and thermodynamic modeling, Acta Materialia 108 (2016) 46-54, https://doi.org/10.1016/j.actamat.2016.02.019.
[3] Y. Wen, B. Zhang, R.L. Narayan, P. Wang, X. Song, H. Zhao, U. Ramamurty, X. Qu, Laser powder bed fusion of compositionally graded CoCrMo-Inconel 718, Addit. Manuf. 40 (2021) 101926, https://doi.org/10.1016/j.addma.2021.101926.
[4] W. Liu, J. DuPont, Fabrication of functionally graded TiC/Ti composites by laser engineered net shaping, Scripta Mater. 48 (2003) 1337-1342, https://doi.org/10.1016/S1359-6462(03)00020-4
[5] P. Morgand, P. Mouturat, G. Sainfort, Structure and mechanical properties of iron-aluminium alloys, Acta Metall. 16 (1968) 867-875, https://doi.org/10.1016/0001-6160(68)90107-7.
[6] M. Marcinkowski, M. Taylor, F. Kayser, Relationship between atomic ordering and fracture in Fe-Al alloys, J. Mater. Sci.10 (1975) 406-414, https://doi.org/10.1007/BF00543684.
[7] M. Palm, F. Stein, G. Dehm, Iron aluminides, Annu. Rev. Mater. Res. 49 (2019) 297-326, https://doi.org/10.1146/annurev-matsci-070218-125911.
[8] J. Herrmann, G. Inden, G. Sauthoff, Deformation behaviour of iron-rich iron-aluminum alloys at low temperatures, Acta Mater. 51 (2003) 2847-2857, https://doi.org/10.1016/S1359-6454(03)00089-2.
[9] B. Song, S. Dong, P. Coddet, H. Liao, C. Coddet, Fabrication and microstructure characterization of selective laser-melted FeAl intermetallic parts, Surf. Coat. Tech.206 (2012)

4704-4709, https://doi.org/10.1016/j.surfcoat.2012.05.072.
[10] T. Hauser, P.P. Breese, T. Kamps, C. Heinze, J. Volpp, A.F.H. Kaplan, Material transitions within multi-material laser deposited intermetallic iron aluminides, Addit. Manuf. 34 (2020) 101242, https://doi.org/10.1016/j.addma.2020.101242.
[11] M. Pęska, K. Karczewski, M. Rzeszotarska, M. Polański, Direct Synthesis of Fe-Al Alloys from Elemental Powders Using Laser Engineered Net Shaping, Materials 13 (2020) 531, https://doi.org/10.3390/ma13030531
[12] J.H. Martin, B.D. Yahata, J.M. Hundley, J.A. Mayer, T.A. Schaedler, T.M. Pollock, 3D printing of high-strength aluminium alloys, Nature 549 (2017) 365-369, https://doi.org/10.1038/nature23894.
[13] C. Shen, M. Reid, K.-D. Liss, Z. Pan, Y. Ma, D. Cuiuri, S. van Duin, H. Li, Neutron diffraction residual stress determinations in Fe3Al based iron aluminide components fabricated using wire-arc additive manufacturing (WAAM), Addit. Manuf. 29 (2019) 100774, https://doi.org/10.1016/j.addma.2019.06.025.
[14] X. Tan, Y. Kok, Y.J. Tan, M. Descoins, D. Mangelinck, S.B. Tor, K.F. Leong, C.K. Chua, Graded microstructure and mechanical properties of additive manufactured Ti–6Al–4V via electron beam melting, Acta Mater. 97 (2015) 1-16, https://doi.org/10.1016/j.actamat.2015.06.036.
[15] C. Shen, Z. Pan, D. Cuiuri, J. Roberts, H. Li, Fabrication of Fe-FeAl functionally graded material using the wire-arc additive manufacturing process, Metall. Mater. Trans. B 47 (2016) 763-772, https://doi.org/10.1007/s11663-015-0509-5.
[16] N. Kang, P. Coddet, H. Liao, T. Baur, C. Coddet, Wear behavior and microstructure of hypereutectic Al-Si alloys prepared by selective laser melting, Appl. Surf. Sci. 378 (2016) 142-149, https://doi.org/10.1016/j.apsusc.2016.03.221.
[17] F. Stein, M. Palm, Re-determination of transition temperatures in the Fe–Al system by differential thermal analysis, Int. J. Mater. Res., 98 (2007) 580-588, https://doi.org/10.3139/146.101512.
[18] W. Koester, Physical measurements of iron-aluminum alloys with 10 to 50 at.-% Al. IV. Young's modulus of the alloys, Z. Metallkd 73 (1982) 111–114.
[19] S. Das, Physical aspects of process control in selective laser sintering of metals, Adv. Engin. Mater. 5 (2003) 701-711, https://doi.org/10.1002/adem.200310099
[20] P. Kumar, O. Prakash, U. Ramamurty, Micro-and meso-structures and their influence on mechanical properties of selectively laser melted Ti-6Al-4V, Acta Mater. 154 (2018) 246-260, https://doi.org/10.1016/j.actamat.2018.05.044.
[21] T. DebRoy, H.L. Wei, J.S. Zuback, T. Mukherjee, J.W. Elmer, J.O. Milewski, A.M. Beese, A. Wilson-Heid, A. De, W. Zhang, Additive manufacturing of metallic components – Process, structure and properties, Prog. Mater. Sci. 92 (2018) 112-224, https://doi.org/10.1016/j.pmatsci.2017.10.001.
[22] W.A. Tiller, K.A. Jackson, J.W. Rutter, B. Chalmers, The redistribution of solute atoms during the solidification of metals, Acta Metall. 1 (1953) 428-437, https://doi.org/10.1016/0001-6160(53)90126-6.
[23] S. Kou, Welding metallurgy, New Jersey, USA (2003) 431-446,
[24] M. Gäumann, C. Bezençon, P. Canalis, W. Kurz, Single-crystal laser deposition of superalloys: processing–microstructure maps, Acta Mater. 49 (2001) 1051-1062, https://doi.org/10.1016/S1359-6454(00)00367-0.
[25] W. Kurz, B. Giovanola, R. Trivedi, Theory of microstructural development during rapid solidification, Acta Metall. 34 (1986) 823-830, https://doi.org/10.1016/0001-6160(86)90056-8.
[26] H.L. Wei, J.W. Elmer, T. DebRoy, Origin of grain orientation during solidification of an aluminum alloy, Acta Mater. 115 (2016) 123-131, https://doi.org/10.1016/j.actamat.2016.05.057.
[27] D. Zhang, D. Qiu, M.A. Gibson, Y. Zheng, H.L. Fraser, D.H. StJohn, M.A. Easton, Additive manufacturing of ultrafine-grained high-strength titanium alloys, Nature 576 (2019) 91-95, https://doi.org/10.1038/s41586-019-1783-1
[28] A.M. Mitrašinović, F.C. Robles Hernández, Determination of the growth restriction factor and grain size for aluminum alloys by a quasi-binary equivalent method, Mater. Sci. Engin. A

540 (2012) 63-69, https://doi.org/10.1016/j.msea.2012.01.072.
[29] M.Y. Mendoza, P. Samimi, D.A. Brice, B.W. Martin, M.R. Rolchigo, R. LeSar, P.C. Collins, Microstructures and Grain Refinement of Additive-Manufactured Ti-x W Alloys, Metall. Trans. A, 48 (2017) 3594-3605, https://doi.org/10.1007/s11661-017-4117-7
[30] Y.-Y. Zhu, H.-B. Tang, Z. Li, C. Xu, B. He, Solidification behavior and grain morphology of laser additive manufacturing titanium alloys, J. Alloys Compd. 777 (2019) 712-716, https://doi.org/10.1016/j.jallcom.2018.11.055.
[31] Kurz, W. & Fisher, D. J. Fundamentals of Solidification 3rd ed, Trans Tech Publications, 1989.
[32] J. Gao, S. Jiang, H. Zhang, Y. Huang, D. Guan, Y. Xu, S. Guan, L.A. Bendersky, A.V. Davydov, Y. Wu, Facile route to bulk ultrafine-grain steels for high strength and ductility, Nature 590 (2021) 262-267, https://doi.org/10.1038/s41586-021-03246-3.
[33] E. Frutos, D.G. Morris, M.A. Muñoz-Morris, Evaluation of elastic modulus and hardness of Fe–Al base intermetallics by nano-indentation techniques, Intermetallics 38 (2013) 1-3, https://doi.org/10.1016/j.intermet.2013.02.012.